Journal of Visualization, Vol. 8, No. 1 (2005)9-21

Thermal and Flow Characteristics of Evaporating Capillary Pore Flows Ranging from 10-mm to 10-μm Diameter

Kim, H. J.[*1] and Kihm, K. D.[*2]

*1 Division of Mechanical Engineering, Ajou University, Wonchon-Dong, Suwon, 442-749, Korea.
E-mail: hyunkim@ajou.ac.kr
*2 Mechanical, Aerospace and Biomedical Engineering, University of Tennessee, Knoxville, TN 37996 2210, USA.

Received 27 August 2004
Revised 14 October 2004

Abstract : Flow and thermal characteristics are studied for capillary pore cavities with free surfaces ranging from 10-mm to 10-μm diameter. Also the effect of micro gravity is investigated. A standard finite volume method (FVM), in association with the well-established boundary-fitted coordinate transformation (BFCT), is used to numerically solve the governing equations for primitive scalar variables of velocity components, pressure and temperature. Calculation results show that the convection-driven circulation and the thermocapillary phoresis effect dominate the flow and thermal fields of larger pores, bigger than 1.0-mm diameter. With decreasing pore diameter, the flow circulation diminishes and the interfacial evaporation dominates to establish nearly stratified flow patterns parallel to the pore wall. Micro-scale capillary pores, less than 1.0-mm diameter, show no flow circulation with almost horizontally stratified temperature fields. Micro gravity condition shifts this transition which is from convection-driven to interfacial flow dominated flow regime to bigger pore diameter.

Keywords : Thermocapillary, Microscale, Meniscus, Evaporation, Buoyancy.

Nomenclature

C_0, C_1	Constant for surface tension
e	Accommodation coefficient
g	Acceleration to gravity
j	Mass flux
k	Thermal conductivity
L	Latent heat
M_w	Molecular weight
P_d	Dynamic pressure
R_g	Universal gas constant
t	Time
T	Temperature
V_i	i-direction velocity
Γ	Thermal diffusivity
x, y, z	Coordinate system of physical domain
ξ,η,ζ	Coordinate system of computational domain

Subscript

i	Derivative with respect to I – direction
l	Lowest temperature
0	Surrounding vapor temperature

Superscript

v	Vapor
s	Surface

W	Contact angle
α	Contact angle of meniscus surface
ρ	Density
β	Expansion coefficient
κ	Surface curvature
γ	Surface tension
τ_{ij}	Viscous stress tensor

Dimensionless parameter

Bo	Bond number	$\left[\frac{\rho g D^2}{\gamma}\right]$
Cr	Crispation number	$\left[\frac{1}{\gamma}\left\|\frac{\partial\gamma}{\partial T}\right\|\|\Delta T\|\right]$
Ma	Marangoni number	$\left[\frac{\left\|\frac{\partial\gamma}{\partial T}\right\|\|\Delta T\|D}{\mu\alpha}\right]$

1. Introduction

Two-phase heat transfer has received revived attention since a large amount of latent heat transport can be an effective cooling (or warming) means for highly intense heat generating devices such as modern electronics and avionics, temperature equalization of spatial structure, or deicing of aircraft surfaces. Representatives using latent heat transport, between liquid and vapor phases, are heat pipes and capillary pumping loops (Peterson, 1994). The former consists of micro-porous wicking structures to circulate the internal working fluid by capillary pressure. In the latter the capillary pumping potential, created by the micro-scale evaporator pore and larger scale condenser pore, pumps the working fluid from the condenser to the evaporator. The evaporator sections of both cases are comprised of micro-scale liquid-vapor interfaces that can be simplified and modeled by a micro-scale evaporating capillary pore.

The flow inside an evaporating capillary pore is described by the combined action of buoyancy drive, primarily in the bulk pore, and thermocapillary stress drive, dominant at the interface. In addition, in the case of a steady operation, the mass balance between the evaporation flux at the interface and induced liquid flow rate from the pore bottom will complete the mass transport inside. The energy balance determines the temperature distribution along the interface as well as inside the pore and the amount of heat transfer is assumed to balance with the latent heat removed by evaporation, in the case of a steady operation. In practice, the dependence of the meniscus wetting characteristics on temperature may constitute a moving boundary problem.

Detailed knowledge of heat and mass transport through micro-scale evaporating menisci is crucial to understanding the physics of two-phase heat transport devices and to facilitate further attempts to augment heat transfer efficiency. Flow and thermal characteristics of micro-scale pore should be significantly different from those of meso-scale pores. With decreasing pore dimension, the ratio of gravitational to surface tension forces (Bond number) decreases and the ratio of thermocapillary stress to buoyancy forces (represented by the ratio of Marangoni number to Rayleigh number) increases rapidly. Examination of flow velocity and temperature profiles will be necessary to understand the dependence of capillary pore heat and mass transport on the pore dimension.

The general area of thermocapillary and buoyancy driven flow thermal physics has been extensively studied by a number of researchers. To the authors' knowledge, however, published results are scarce for the heat and mass transport of evaporating micro-scale capillary pores. A steady thermocapillary-driven flow inside a square two-dimensional cavity was studied to simulate material processing (Carpenter and Homsy, 1990). A finite difference method was used to solve the constitutive equations, in the absence of evaporating meniscus. The effect of thermocapillary convection within a two-dimensional cavity, with the meniscus present, was examined by considering both wetting and non-wetting liquid with fixed meniscus shapes (Keller and Bergman,

1990). Chen et al. (1990) studied a cavity flow driven by both thermocapillary and buoyancy forces by solving the Navier-Stokes equation and the energy equation using a finite-difference method associated with a boundary-fitted curvilinear coordinate system. They determined the shape of the meniscus iteratively with a given pore height and a fixed contact angle. Also a transient case of thermocapillary and buoyancy driven flows in a cavity has been numerically studied by several researchers (Ahmed et al., 1997, and Pan et al., 1998). Schmidt et al. (1995A) investigated the evaporation effect on meniscus and presented a range of parametric study of thermal and flow fields using a finite element method. Their study also investigated two-dimensional cavity flows.

Lan and Kou (1991) examined a cylindrical cavity problem using a finite volume method, but restricted their calculations to the zero-gravity case for which buoyancy-driven flow is absent. More recently, the cylindrical pore problem has been addressed (Zhang et al., 1992, and Chen et al., 1998). These studies also considered a moderate scale problem. Mundarne and Zebib (1993) analyzed a three-dimensional flow driven by buoyant thermocapillary convection in a cubic cavity. Similar observations were conducted by Behnia et al. (1995), who also tackled the three-dimensional cubic cavity flows for a wider range of parameters. However, their solutions were obtained for a flat meniscus assuming no curvature effect, being far from representing any small or micro-scale dimensional phenomena. Sefiane et al. (2004) studied the evaporating meniscus at the exit of a capillary experimentally and numerically. Their result showed that as the volatility of a liquid or a series of liquids rises, the increase of evaporation changes the shape of the meniscus through its effect on the interface surface tension.

The purpose of this work is to investigate the effect of pore diameter, ranging from 10-mm to 10 μm, and the effect of varying the gravity on thermal and flow characteristics inside the capillary pore, which are driven by the combined actions of buoyancy, thermocapillary, evaporation and induced convection. A finite volume technique was used to numerically solve the appropriate equations and the computational domain including the concave meniscus was mapped into a rectangular computational domain using a Body Fitted Coordinate Transformation (BFCT) technique.

2. Numerical Formulation

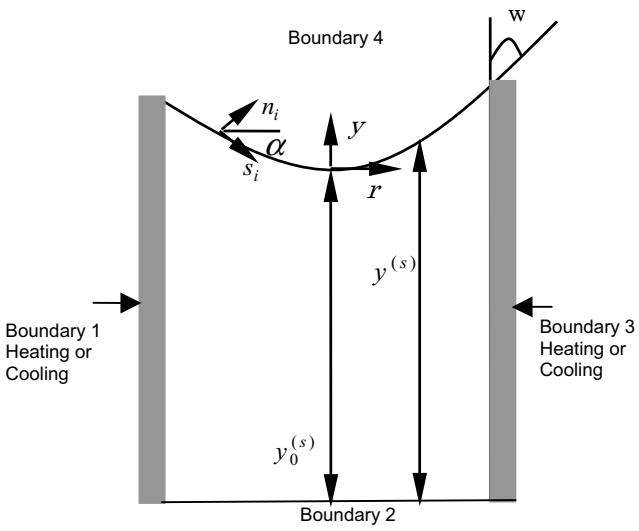

Fig. 1. Problem domain –
(a) case 1: subcooling (b) case 2: superheating.

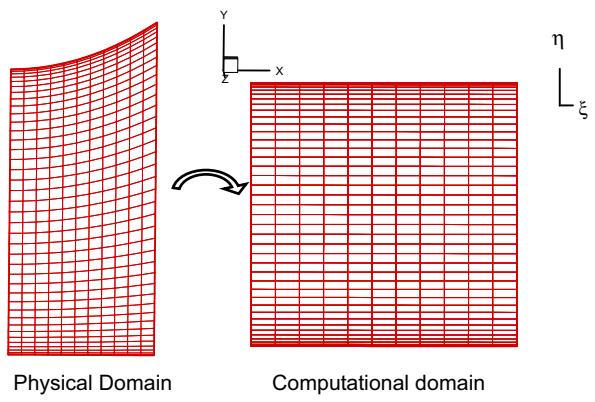

Fig. 2. The body fitted coordinate system for the axisymmertic problem domain.

The physical domain considered for computation is shown in Fig. 1. The pore diameter (D)-to-height (y_o) ratio is set to be 1 and the cylindrical pore ensures axi-symmetric velocity and temperature profiles. A constant temperature heating is provided from the pore wall for superheating and a constant-temperature cooling for subcooling.

The governing equations for velocity, pressure, and temperature are constituted by the continuity, momentum, and energy equations (Slattery, 1981).

Surface tension dependency on temperature is assumed to be linear (Carey, 1992):

$$\gamma = C_0 - C_1 T \tag{1}$$

where C_0 and C_1 are material constants that are available from published data.

In addition to the governing equations, there are several jump boundary conditions that apply along the meniscus surface. The jumping mass balance condition relates the interfacial mass flux to the evaporation and this condition is expressed as (Slattery, 1981):

$$j = \rho^{(v)}\left(V_j^{(v)} - V_j^{(s)}\right)n_j \tag{2}$$

where $V_j^{(v)}$ is the vapor velocity, $V_j^{(s)}$ is the velocity of the interface. Mass continuity requires the evaporative interfacial flow rate at boundary 4 to balance with the mass flow coming through boundary 2. (Schmidt, 1995A)

$$\int_{A_2} \rho_l \overline{V} \cdot d\overline{A} = \int_{A_4} \rho_l \overline{V} \cdot d\overline{A} \tag{3}$$

The well-known Hertz-Knudsen relation (Kennard, 1938) was used to relate the evaporative mass flux to the density differential of the vapor undergoing change to $\rho^{(v)}$ from the surrounding vapor density $\rho_0^{(v)}$:

$$j = e\left\{\frac{R_g T_0}{2\pi M_W}\right\}^{1/2}\left(\rho^{(v)} - \rho_0^{(v)}\right) \tag{4}$$

where e is the accommodation coefficient that is a factor representing the resistance to the evaporative mass transfer. (All present calculations used e = 1.0.) If one treats density as a linear function of temperature, the density difference can be expressed as the following:

$$\rho^{(v)} - \rho_0^{(v)} = \frac{\partial \rho_0^{(v)}}{\partial T}\left(T - T_0\right) \tag{5}$$

From the chain rule:

$$\frac{\partial \rho_0^{(v)}}{\partial T} = \frac{\partial \rho_0^{(v)}}{\partial P}\frac{dP}{dT} \tag{6}$$

Applying the ideal gas equation:

$$\frac{\partial \rho_0}{\partial P} = \frac{M_W}{R_g T_0} \tag{7}$$

Substituting Equations (5) through (7) into (4) and applying the Clapyeron equation gives

$$j = \frac{e\rho_0^{(v)} L}{T_0^{3/2}}\left(\frac{M_W}{2\pi R_g}\right)^{1/2}\left(T - T_0\right) \tag{8}$$

To balance the thermocapillary stress, one can equate the surface tension gradient to the tangential stress on the interface:

$$\tau_{ij} n_j = \gamma_{,i} \tag{9}$$

If one considers the equilibrium of energy on the meniscus equating the heat flux to the transfer of latent heat, the energy jump condition can be obtained:

$$kT_{,i} n_i = jL \tag{10}$$

where j denotes the mass flux given in Eq. (4) and L represents the latent heat amount per unit mass. The velocity boundary conditions on the rigid pore wall (boundary 1 or 3) are:

$$V_i = 0 \tag{11}$$

The superheated condition is specified by the constant pore wall temperature 2°K above the saturation temperature and the subcooled condition is represented by the wall temperature 2°K below the saturation. The bottom surface of the pore (boundary 2) is assumed to have the same temperature as the pore wall for each condition.

Assuming that the meniscus shape change is negligible for the surface temperature variation, the static surface shape was calculated using (Schmidt et al., 1995A, Schmidt, 1994):

$$\kappa = \frac{\rho g}{\gamma} y_0^{(s)} + \frac{\rho g}{\gamma}\int_0^r \tan\alpha dr \tag{12}$$

Though the above assumption of invariant surface shape may not be always true, it is conjectured that a slightly different surface shape should not significantly change the thermal and flow characteristics inside a pore for the present calculation conditions. This assumption will be justified by estimating the proper dimensionless numbers and will be re-discussed in the Results and

Discussion Section.

The physical domain considered has an axi-symmetric curved boundary-meniscus as shown in Fig. 2. In order to use FDM or FVM, the general curvilinear coordinate system (Chuichi, 1994) must be used to fit the curved boundary wall. Now, the physical domain (x, y, z) is mapped to a computational domain (ξ, η, ζ). The governing equations are also transformed into the computational Cartesian coordinate system (ξ, η, ζ).

The finite volume method (Patankar, 1980) was used to iteratively solve the elliptical problem for the dependent variables of *T*, *P*, *u*, *v*, *w*, and simultaneously for the implicit boundary conditions given in Eqs. (2) to (12). By using a boundary fitted curvilinear coordinate system with coordinate lines coincident with the boundaries, the physical domain was mapped to the computational domain. In the transformed rectangular domain, the governing equations and their boundary conditions were discretized on a uniform grid by using the finite volume method. The SIMPLE (Semi-Implicit Method for Pressure-Linked Equation) algorithm is adopted to obtain the pressure field.

The grid dimension was set to 21×41 for the entire calculations. Around 10,000 iterations were required to reach an acceptable convergence that usually takes approximately 15 CPU minutes on the Pentium 4 1.2 GHz PC platform. The relaxation factor for all the variables was set to be 0.5.

3. Results and discussion

Results are presented for velocity vector fields, flow streamlines and isothermal contours for water and Refrigerant-114 as working fluids. Two heating conditions are considered at the 5mm diameter pore wall, 2°K superheated (evaporation) and 2°K subcooled (condensation). All thermodynamic properties are obtained at the saturation state of each fluid at 1 atm.

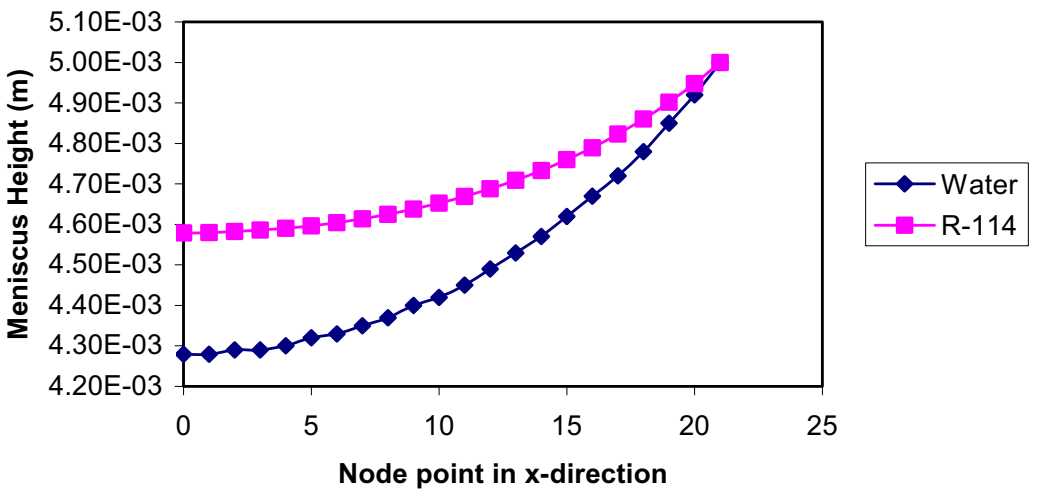

Fig. 3. The Comparison of Static Meniscus Shapes.

Crispation numbers of both tested fluids are very low (Cr = 6.6x10^{-3} for water and 8.9x10^{-3} for R-114) and Biot numbers are high (Bi = 5.77x10^{4} for water and 9.71x10^{4} for R-114). Therefore the surface deformation occurring due to the surface temperature gradient can be considered negligibly small (Schmidt et al., 1995B, Ahmed et al., 1997) and the present calculation uses static menisci. Figure 3 shows the static surface shapes calculated by Eq. (12) with a specified contact angle of 45 degrees for both tested fluids.

Figure 4 shows the effect of capillary pore diameter on the flow and thermal characteristics in the case of superheated water with 15 degrees contact angle. With decreasing pore diameter the thermocapillary drive is reduced and the viscous effect dominates the thermocapillary phoresis along with a decreasing Marangoni number. Decreasing Bond and Rayleigh numbers indicate a reduced gravitational effect and a less buoyant drive, respectively. This reduction of density-driven convection diminishes the flow circulation and the viscous effect overrides the flow circulation and nearly parallel streamlines directed toward the free surface are established for the pore diameters below 1.0-mm. The temperature profile relaxes to horizontal stratification near the pore center, at about 1.0-mm pore diameter. The buoyancy-driven descending flow along the pore center is resisted by the friction drag of the stronger ascending flow along the pore wall and the flow direction is eventually reversed to ascend to the free surface when the pore diameter is reduced to 100 μm. With further decrease in pore diameter, both flow and thermal behavior remains similar, i.e., vertically stratified streamlines and horizontally stratified temperature contours.

The effect of capillary pore diameter for subcooling case is shown in Fig. 5. As it is shown in Fig. 4, weaker flow circulation makes smaller contour deformation for 10-mm and 5-mm pore diameter. Flow circulation is the counter clockwise direction. With decreasing pore diameter, density driven flow decreases and interfacial flow by condensation at the meniscus surface begin to show from 1-mm pore diameter. From 100-μm, the flow regime becomes dominated by interfacial flow by condensation.

Figure 6 shows the evaporation velocity profiles versus pore diameters ranging from 10-mm to 10-μm in superheating case. The evaporative flux dramatically increases approaching the pore wall where the maximum heat transfer and temperature gradient exists.

This is also consistent with the analytical finding that the maximum heat and mass transfer occurs within a micro-scale range of thin film region (Potash and Wayner, 1972, Pratt, 1996). The calculated maximum evaporation velocity at the pore wall persistently increases from 14 μm/s to 4.4 mm/s with the pore diameter reduced from 10-mm to 10-μm. The ratio of the wet perimeter to the pore cross-sectional area can be a measure of heat transfer rate per unit liquid volume contained in the pore and this ratio increases with decreasing pore diameter. The capillary pore with a smaller diameter receives more heat flux per volume of liquid, which in turn increases the evaporation flux. Another reason for the increased evaporation for smaller pores may be attributed to the reduced or diminished flow circulation because of the aforementioned viscous drag of the ascending flow exerted on the descending center flow.

Figure 7 shows the effect of reducing the gravity (0.01g) on the flow and thermal characteristics in the case of superheated water from 10-mm to 10-μm pore diameter with 15 degrees contact angle. Reducing the gravity reduces the buoyancy driven flow. So interfacial flow shows from bigger pore diameter, 5-mm. Micro gravity condition can be considered to have a similar effect with decreasing pore diameter for the flow and thermal characteristics.

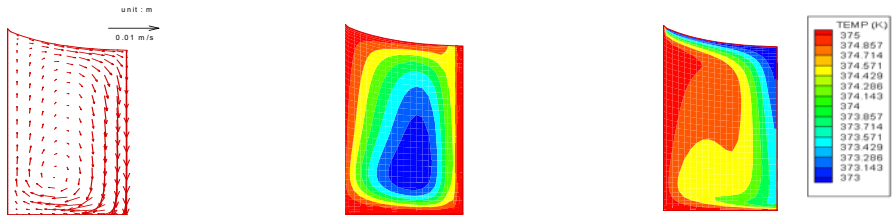

(a) 10mm diameter pore: $Ma = 8.12 \times 10^4$, $Bo = 16.0$, $Ra = 3.04 \times 10^5$

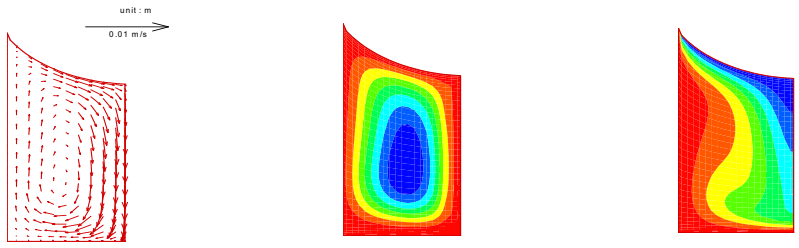

(b) 5mm diameter pore: $Ma = 4.06 \times 10^4$, $Bo = 4.0$, $Ra = 3.8 \times 10^4$

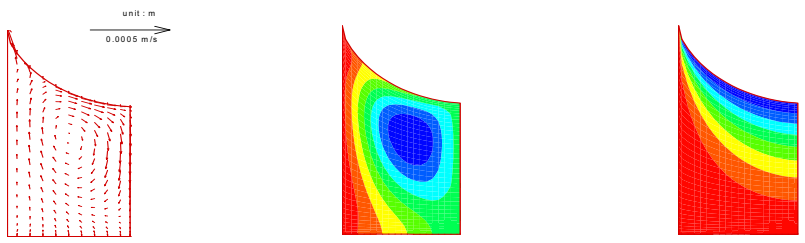

(c) 1mm diameter pore: $Ma = 8.12 \times 10^3$, $Bo = 1.6 \times 10^{-1}$, $Ra = 304.16$

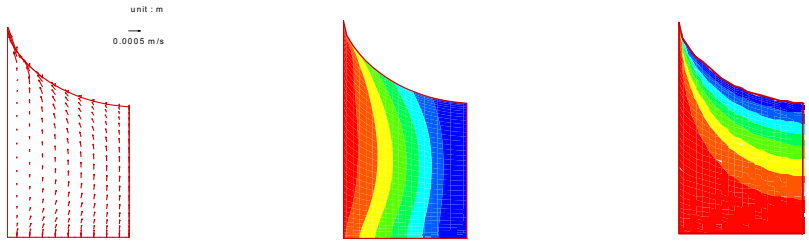

(d) 100 μm diameter pore: $Ma = 812$, $Bo = 1.6 \times 10^{-3}$, $Ra = 3.04 \times 10^{-1}$

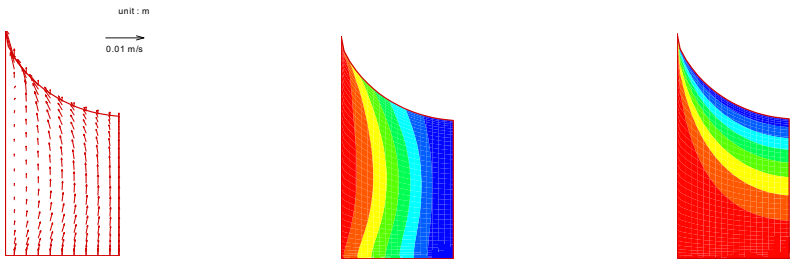

(e) 10 μm diameter pore: $Ma = 81$, $Bo = 1.6 \times 10^{-5}$, $Ra = 3.04 \times 10^{-4}$

Fig. 4. Velocity, Streamline and Temperature Profile for Water: Superheating Case Pore Diameter: 10mm, 5mm, 1mm, 100μm, 10μm.

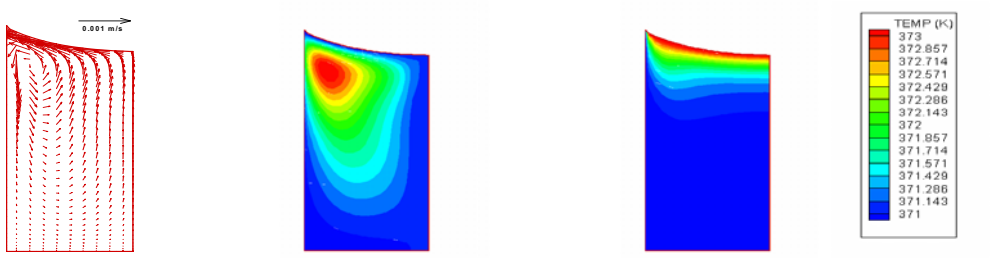

(a) 10mm diameter pore: $Ma = 8.12 \times 10^4$, $Bo = 16.0$, $Ra = 3.04 \times 10^5$

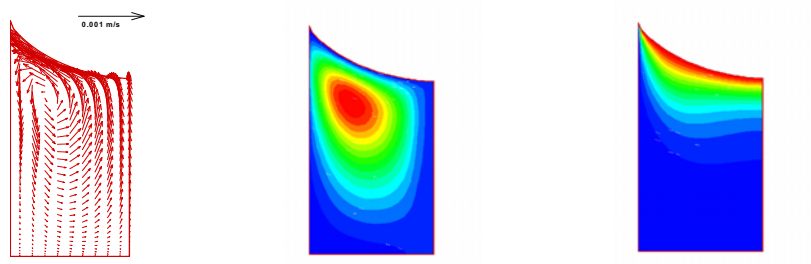

(b) 5mm diameter pore: $Ma = 4.06 \times 10^4$, $Bo = 4.0$, $Ra = 3.8 \times 10^4$

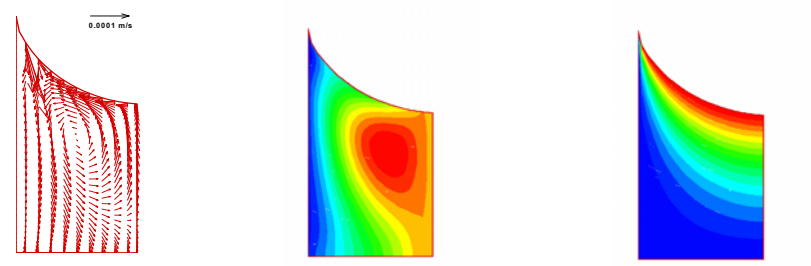

(c) 1mm diameter pore: $Ma = 8.12 \times 10^3$, $Bo = 1.6 \times 10^{-1}$, $Ra = 304.16$

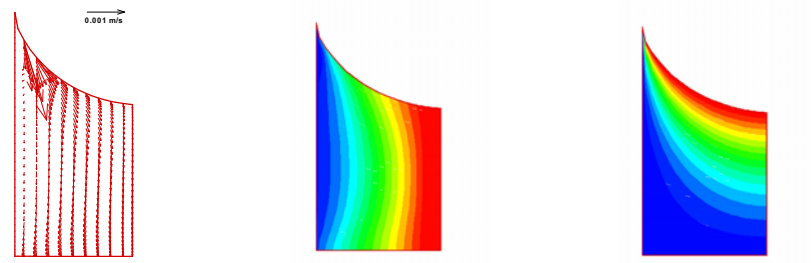

(d) 100 μm diameter pore: $Ma = 812$, $Bo = 1.6 \times 10^{-3}$, $Ra = 3.04 \times 10^{-1}$

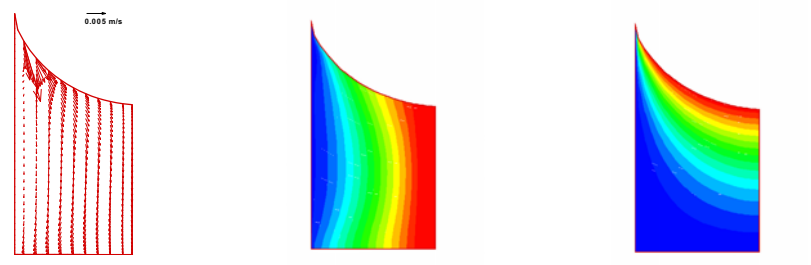

(e) 10 μm diameter pore: $Ma = 81$, $Bo = 1.6 \times 10^{-5}$, $Ra = 3.04 \times 10^{-4}$

Fig. 5. Velocity, Streamline and Temperature Profile for Water: Subcooling Case Pore Diameter: 10mm, 5mm, 1mm, 100μm, 10μm.

Figure 8 presents the magnitudes of the highest flow velocities for the range of pore diameters for superheated water. For the buoyancy-convection dominating region of pore diameters larger than 1.0-mm with normal gravity, the highest velocity occurs from the recirculating flow field and the evaporation velocities are order-of-magnitudes smaller as shown in Fig. 6. The reduced dimension and strength of the recirculating flow with decreasing pore diameter decreases the maximum velocity and the lowest maximum velocity is reached when the recirculation is ceased by the overriding viscous effect at around D = 1.0-mm. However, with micro gravity condition, the magnitudes of recirculating flow are much smaller than the interfacial evaporation flow because density-driven flow is restricted. So the plotting line seems to be flat.

Below 1.0-mm pore diameter of both conditions, the maximum velocity corresponds to the maximum evaporation velocity that increases with decreasing pore diameter as discussed previously. Figure 9 shows the highest flow velocities for subcooled water. The case of subcooled water has similar pattern to superheated water one. However, as discussed previously, due to the weaker buoyancy-driven flow in subcooled water, the moderate slope of velocity in larger than 1.0-mm pore diameter is showed.

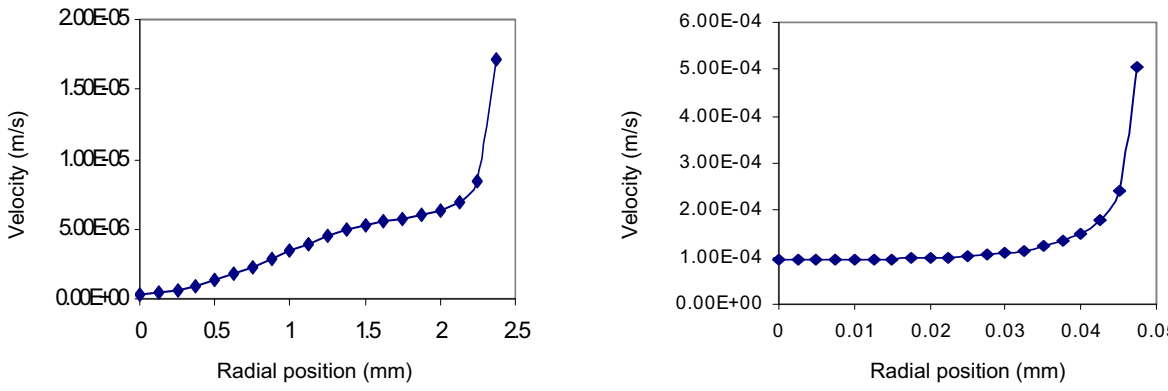

Fig. 6. Evaporation Velocity on the Surface for Water: Superheating Case Pore Diameter: 5mm, 100μm.

4. Conclusion

The velocity and temperature profile inside the capillary pore with an evaporating surface was calculated by using FVM technique. Results showed that the flow and temperature pattern results from the competition of buoyancy, thermocapillary and interfacial flow. In larger pores, bigger than 1.0-mm diameter ($Ma = 8.12 \times 10^{3}$, $Bo = 1.6 \times 10^{-1}$, $Ra = 304.16$), the flow and temperature field is dominated by buoyancy and thermocapillary phoresis which shows the circulation flow. However, with decreasing pore diameter less than 1.0 mm ($Ma = 8.12 \times 10^{3}$, $Bo = 1.6 \times 10^{-1}$, $Ra = 304.16$), the capillary pore begins to be the interfacial evaporation dominant. The flow pattern becomes being stratified, diminishing flow circulation. And Micro gravity condition showed a similar effect with decreasing pore diameter for the flow and thermal characteristics. It is concluded that the liquid inside a capillary pore is dominated by different regime – thermocapillary, buoyancy or evaporation, depending on pore diameters and micro gravity condition.

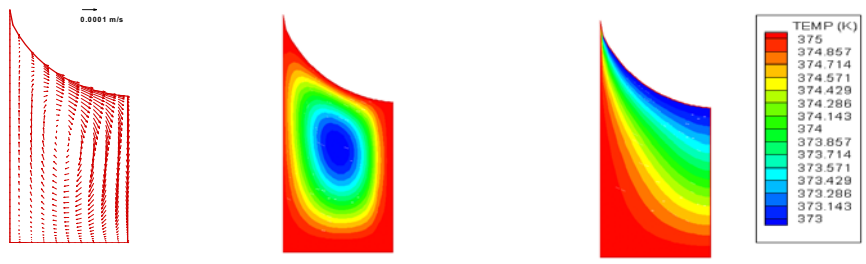

(a) 10mm diameter pore: $Ma = 8.12 \times 10^4$, $Bo = 0.16$, $Ra = 3.04 \times 10^3$

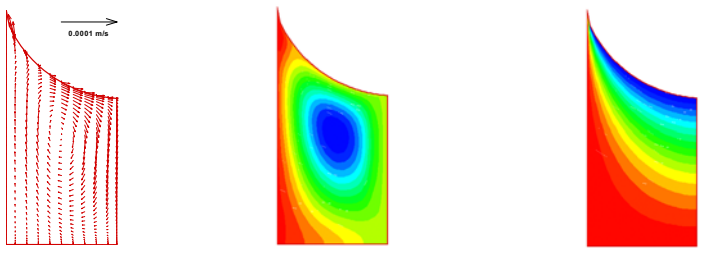

(b) 5mm diameter pore: $Ma = 4.06 \times 10^4$, $Bo = 0.04$, $Ra = 3.8 \times 10^2$

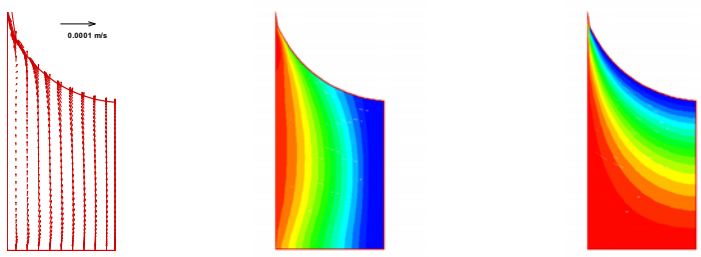

(c) 1mm diameter pore: $Ma = 8.12 \times 10^3$, $Bo = 1.6 \times 10^{-3}$, $Ra = 3.04$

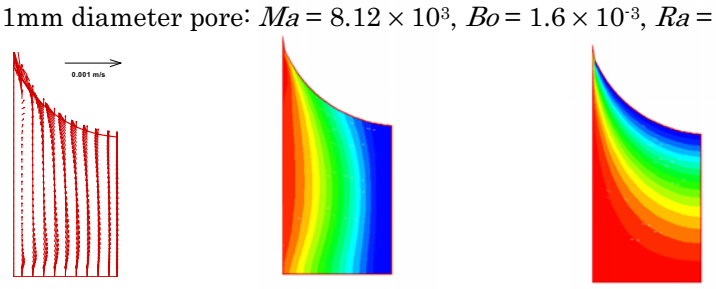

(d) 100 μm diameter pore: $Ma = 812$, $Bo = 1.6 \times 10^{-5}$, $Ra = 3.04 \times 10^{-3}$

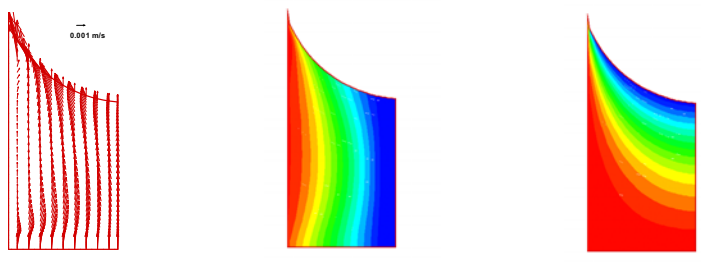

(e) 10 μm diameter pore: $Ma = 81$, $Bo = 1.6 \times 10^{-7}$, $Ra = 3.04 \times 10^{-6}$

Fig. 7. Micro Gravity (0.01g) Velocity, Streamline and Temperature Profile for Water: Superheating Case, Pore Diameter: 10mm, 5mm, 1mm, 100μm, 10μm.

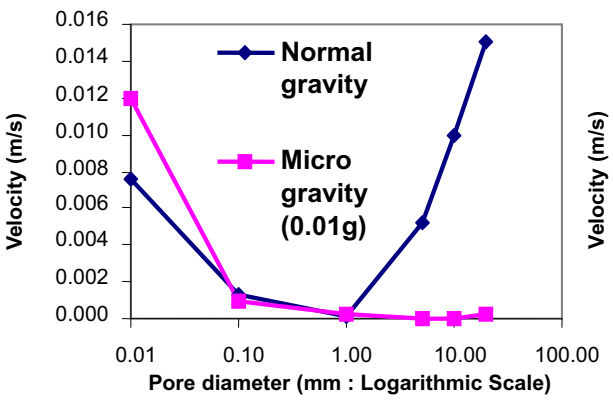

Fig. 8. Maximum Velocity For Water: Superheating Case, Pore Diameter: 20mm, 10mm, 5mm, 1mm, 100μm, 10μm.

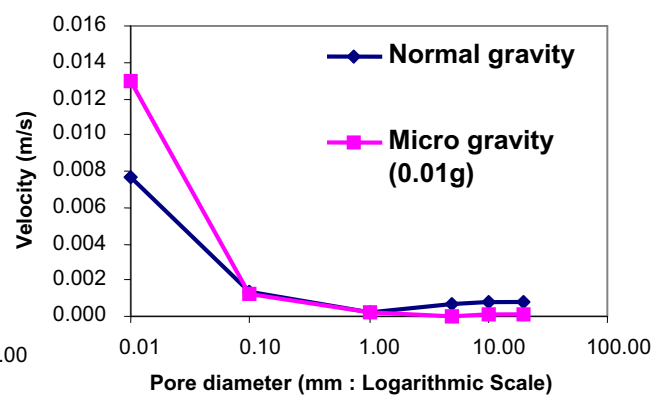

Fig. 9. Maximum Velocity For Water: Subcooling Case, Pore Diameter: 20mm, 10mm, 5mm, 1mm, 100μm, 10μm.

Acknowledgements

This material is based on the work supported by the grant of Ajou University and the National Research Laboratory (Thermo-mechanical Properties Measurement Laboratory), established by Korea Institute Science and Technology Evaluation and Planning.

References

Ahmed, I. and Ball, K. S., Spectral Simulation of Thermocapillary Convection wiith Deformable Free Surface Using Boundary-Fitted Coordinates, Numerical Heat Transfer, Part B, 32 (1997), 127-149.

Carey, V. P., Liquid-Vapor Phase-Change Phenomena, (1992), Taylor & Francis.

Carpenter, B. M. and Homsy, G. M., High Marangoni Number Convection in a Square Cavity: Part II, Phys. Fluid A 2-2 (1990-2) 137-149.

Chen, J. C., Sheu, J. C. and Jwu, S. S., Numerical Computation of Thermocapillary Convection in a Rectangular Cavity, Numerical Heat Transfer, Part A, 17 (1990), 287-308.

Chen, Y., David, S. A. and Zacharia, T., Marangoni, Convection with Two Free Surfaces, Numerical Heat Transfer, Part A, 33 (1991), 599-620.

Chuichi, A., Computational Fluid Dynamics for Engineering, (1994), University of Tokyo Press.

Keller, J. R. and Bergman, T. L., Thermocapillary Cavity convection in Wetting and Nonwetting Liquids, Numerical Heat Transfer, Part A, 18 (1990), 33-49.

Kennard, E., Kinetic Theory of Gases, (First Edition), (1938), McGraw-Hill, New York, NY.

Lan, C. W. and Kou, S., Heat Transfer, Fluid and Interface Shaped in Floating-zone Crystal Growth, Journal of Crystal Growth, 108 (1991), 351-366.

Mundarne, M. and Zebib, A., Two- and Three-dimensional Buoyant Thermocapillary Convection, Phys. Fluids A 5-4 (1993-4), 810-818.

Pan, D., Yang, Y. -S. and Chang, C. -H., Computation of Internal Flow with Free Surfaces Using Artificial Compressibility, Numerical Heat Transfer, Part B, 33 (1998), 119-134.

Patankar, S. V., Numerical Heat Transfer and Fluid Flow, (1980), Taylor & Francis.

Peterson, G. P., An Introduction to Heat Pipes: Modeling, Testing and Applications, (1994), Wiley, New York.

Potash, M. and Wayner, P. C., Evaporation from a Two-Dimensional Extended Meniscus, Int. J. Heat Mass Transfer, 15 (1972), 1851-1863.

Pratt, D. M., The effects of thermocapilly stresses on the wetting characteristics, heat transfer effectiveness and stability of an evaporating capillary re-supplied curved meniscus within a capillary tube, (1996), Ph.D. Dissertation.

Schmidt, G. R., Chung, T. J. and Nadarajah, A., Thermocapillary Flow with Evaporation and Condensation at Low Gravity. Part 1 Non-deforming surface, Journal of Fluid Mechanics, 294 (1995A), 323-347.

Schmidt, G. R., Chung, T. J. and Nadarajah, A., Thermocapillary Flow with Evaporation and Condensation at Low Gravity. Part 2 Deformable surface, Journal of Fluid Mechanics, 294 (1995B), 349-366.

Schmidt, G. R., Thermocapillary Flow with Evaporation and Condensation and its Effect on Liquid Retention in Low-G Fluid Acquisition Devices, NASA Technical Paper 3463 (1994) 38-120.

Slattery, J. C., Momentum, Energy, and Mass Transfer in Continua, (Second Edition), (1981), Krieger Publishing, Huntington, NY.

Sefiane, K., Snodgrass, M. and Steinchen, A., Evaporation Self-induced Marangoni Motion in Fed Capillaries for Volatile Liquids in Open Air, J. Non-Equilib. Thermodyn. 29 (2004), 177-198.

Stella, M. F. and Guj, G., Numerical Study of Three-Dimensional Low-Pr Buoyancy and Thermocapillary Convection, Numerical Heat Transfer, Part A, 27 (1995), 73-88.

Zhang, Y. and Alexander, J. I. D., Surface Tension and Buoyancy-Driven Flow in a Non-Isothermal Liquid Bridge, International Journal for Numerical Methods in Fluids, 14 (1992), 197-215.

Author Profile

HyunJung Kim: He received his M.S. degree in Mechanical Engineering in 1996 from Hanyang University. He received his Ph.D. in Mechanical Engineering in 2001 from Texas A&M University. He worked as a research associate in Nuclear Engineering Research Laboratory in 2002. He works in Mechanical Engineering, Ajou University as an assistant professor since 2003. His research interests are micro-scale heat and mass transfer and measurement in MEMS and Bio Chips with Micro PIV, LIF.

Kenneth D. Kihm: He received his M.S. degree in Mechanical Engineering in 1981 from Seoul National University. He received his Ph.D. in Mechanical Engineering in 1987 from Stanford University. He worked as a professor in Mechanical Engineering, Texas A&M University until 2004. He currently works as a Magnavox Professor in Mechanical, Aerospace and Biomedical Engineering, University of Tennessee Mechanical Engineering. His research interests are Development and Applications of Optical Diagnostic and Visualization Techniques for Micro/Nano-Scale Fluidic and Thermal Transport.